Ultrafast Science
A SCIENCE PARTNER JOURNAL

Research Article

Exploring Femtosecond Laser Ablation by Snapshot Ultrafast Imaging and Molecular Dynamics Simulation

Jiali Yao,[1] **Dalong Qi,**[1] **Hongtao Liang,**[1] **Yilin He,**[1] **Yunhua Yao,**[1] **Tianqing Jia,**[1] **Yang Yang** ,[1] **Zhenrong Sun,**[1] **and Shian Zhang** [1,2,3]

[1]*State Key Laboratory of Precision Spectroscopy, School of Physics and Electronic Science, East China Normal University, Shanghai 200241, China*
[2]*Collaborative Innovation Center of Extreme Optics, Shanxi University, Taiyuan 030006, China*
[3]*Collaborative Innovation Center of Light Manipulations and Applications, Shandong Normal University, Jinan 250358, China*

Correspondence should be addressed to Yang Yang; yyang@phy.ecnu.edu.cn and Shian Zhang; sazhang@phy.ecnu.edu.cn

Femtosecond laser ablation (FLA) has been playing a prominent role in precision fabrication of material because of its circumvention of thermal effect and extremely high spatial resolution. Molecular dynamics modeling, as a powerful tool to study the mechanism of femtosecond laser ablation, still lacks the connection between its simulation results and experimental observations at present. Here we combine a single-shot chirped spectral mapping ultrafast photography (CSMUP) technique in experiment and a three-dimensional two-temperature model-based molecular dynamics (3D TTM-MD) method in theory to jointly investigate the FLA process of bulky gold. Our experimental and simulated results show quite high consistency in time-resolved morphologic dynamics. According to the highly accurate simulations, the FLA process of gold at the high laser fluence is dominated by the phase explosion, which shows drastic vaporized cluster eruption and pressure dynamics, while the FLA process at the low laser fluence mainly results from the photomechanical spallation, which shows moderate temperature and pressure dynamics. This study reveals the ultrafast dynamics of gold with different ablation schemes, which has a guiding significance for the applications of FLA on various kinds of materials.

1. Introduction

Since the invention of femtosecond solid-state laser in 1991 [1], femtosecond laser ablation (FLA) has become a very active research area [2–4]. In the laser-material interaction process, a femtosecond laser pulse with ultrahigh peak power can deliver its energy to the material in ultrashort time scale before thermal diffusion occurs, and therefore the heat-affected zone is very small, which has the ability to fabricate almost any materials with extremely high precision and minimal collateral damage [5]. Moreover, due to the advantages of no plasma shielding, low ablation threshold and high processing efficiency, FLA has been widely used in various fields of industrial production, such as surface nanostructuring [6], micromachining [7], surface cleaning [8], welding [9], and drilling [10].

Gold, as a precious metal, has aroused tremendous interests of people for thousands of years because of its rare prod-ucts and unique luster. Meanwhile, based on good electrical and thermal conductivity, chemical resistance, strong ductility, and biocompatibility, gold has also played an important role in scientific research and technical applications. In addition, the rapid development of ultrashort laser technique provides an opportunity for further functionalization of gold surface. For example, gold nanoparticles prepared by FLA can be applied to molecular detection [11, 12], nanomedicine [13, 14], and biosensors [15]. Transmission and reflection gratings can be generated by ablating the gold surface via femtosecond laser interferometry [16, 17]. It is necessary to comprehensively understand the fundamental knowledge in the laser-material interaction in order to improve the controllability of the FLA process for various related applications. To this end, a large number of experiments and theories have been conducted to explore FLA of gold. In experiment, a pump-probe technique with high temporal resolution and long temporal range has become the main methods to observe FLA of

gold [18–21]. For example, Wortmann et al. conducted a pump-probe experiment to observe the formation of nano-bumps and nanojets on thin gold film by single femtosecond laser pulse irradiation [18]. Carrasco-García et al. used a pump-probe femtosecond microscopy to observe the formation of dynamic Newton's rings on the gold surface during the FLA process and quantified the radial expansion velocity of molten material [19]. Pflug et al. employed a pump-probe reflectometry and ellipsometry to measure the temporal modification of complex refractive index and relative reflectance of gold after the irradiation with a femtosecond laser pulse [20]. Cheng et al. investigated the ultrafast dynamics of periodic ripples on the surface of a gold film with a prefabricated nano-groove irradiated by single femtosecond laser pulse based on a collinear pump-probe imaging method [21]. In theory, two-temperature model (TTM), hydrodynamic model (HDM), molecular dynamics (MD), and even hybrid models have been developed to illustrate the laser-metal interaction process [22–26]. Jia et al. investigated the ablation depth, threshold fluence, residual thermal energy, and melting layer thickness of aluminum, copper, and gold under different laser parameters based on an improved TTM [22]. Zhao et al. used a two-dimensional (2D) HDM to study the ablation of aluminum by a femtosecond laser pulse, and the ablation rates in vacuum and air were compared over a wide range of laser fluences [23]. Lorazo et al. investigated the mechanisms of laser ablation on silicon with the laser energy being close to the ablation threshold for femtosecond and picosecond laser pulses via MD simulations [24]. Furthermore, to simulate the electronic excitation under the ultrashort laser irradiation at the atomic level, a TTM-based MD (TTM-MD) method was developed for studying the FLA process [25, 26]. Generally, TTM can only describe the electron and lattice temperatures of materials. Compared with HDM, MD simulations are more realistic, which can track the movement of each molecule or atom, and therefore the detailed ablation and phase transition after the femtosecond laser pulse irradiation can be well revealed.

On the one hand, the pump-probe technique has been widely used to observe and understand the materials ablated by the ultrafast laser, but it requires multiple measurements to obtain the spatiotemporal information. The substantial shot-to-shot variations of laser pulses and the nonuniformity of material compositions greatly degrade the detection accuracy. In response, many snapshot ultrafast optical imaging (UOI) techniques have been developed, including sequentially timed all-optical mapping photography (STAMP) [27, 28] or ultrafast framing cameras [29] for direct imaging and compressed ultrafast photography (CUP) [30] for reconstruction imaging. Generally, direct imaging techniques have high spatial resolution but limited sequence depth (i.e., the number of frames per exposure), while reconstruction imaging techniques such as CUP have large sequence depth but suffer from low spatial resolution. It is worth noting that the sequence depth of the STAMP-series techniques has increased from 6 to 25 with the aid of spectral filtering (SF) [31], and SF-STAMP has manifested itself in real-time recording of femtosecond laser induced plasma and shockwave generations in material [32]. Therefore, snapshot UOI techniques have shown indispensable potential in FLA observation. On the other hand, MD simulations generally ignore any effects related to the lateral variation of laser energy deposition and only study the evolution of atomic configurations at different depths along the laser incidence direction [33, 34]. Currently, the three-dimensional (3D) MD simulations of a system with more than ten million atoms are still very challenging. Although there have been some large-scale MD simulations, these simulations have less connection to the experiments [35, 36]. In general, the majority of studies on the same target focus on either experimental observations or theoretical simulations, there still lacks a joint exploration of the FLA process under coincident conditions. To overcome these shortcomings, here we conduct a single-shot chirped spectral mapping ultrafast photography (CSMUP) to record the transient images of single-pulse FLA on a bulky gold with a temporal range covering about 100 ps. The principle of CSMUP can be found in our previous work [37]. CSMUP utilizes a broadband laser pulse with temporally positive chirp to illuminate the ablation area and employs a hyperspectral camera as an image receiver. Based on the temporal-spectral distribution of the chirped laser pulse, the spatiotemporal dynamics information of the FLA process can be extracted from the collected hyperspectral image data. At present, CSMUP can obtain 25 frames of images in a single exposure, and each frame has an image size of 217×409, which is a technique that is suitable for studying the FLA process of materials. Meanwhile, the FLA process of gold in accordance with the experimental conditions is investigated through theoretical simulations. Here, we develop a 3D TTM-MD method for simulation. In our model, a simulated box larger than the pump laser impacted region is studied, and the time-resolved atomic motions as well as the thermodynamic fields of gold can be observed from 3D view. The simulated results are analyzed in detail and compared with the experimental observations. A comprehensive picture of FLA on gold is established in this work, which can provide guidance for the applications of FLA on various kinds of materials.

2. Materials and Methods

In this experiment, a CSMUP system is used to detect the FLA process of gold, and the experimental arrangement is shown in Figure 1(a) (experimental details are in Supplementary Note 1 and Figures S1–S3). A Ti:sapphire laser amplifier provides the femtosecond laser with central wavelength of 800 nm, pulse width of about 50 fs, and repetition rate of 100 Hz. An electronic shutter is used to obtain a single pulse. The output laser is frequency-doubled via a β-BBO crystal to generate 400 nm laser; then, a 567 nm long-pass dichroic mirror (DM1) separates 400 nm laser from 800 nm laser, and a 450 nm short-pass filter (FL1) is utilized to remove the residual 800 nm laser. The 400 nm laser, which is used as the pump laser with the pulse width of about 100 fs, irradiates the gold surface to induce the ablation. The 800 nm laser is used to generate the probe laser and is first focused by a lens (L1) into water to produce a broadband laser with the wavelength range of about 400-950 nm. The spatial quality of the broadband laser generated by nonlinear effects has been
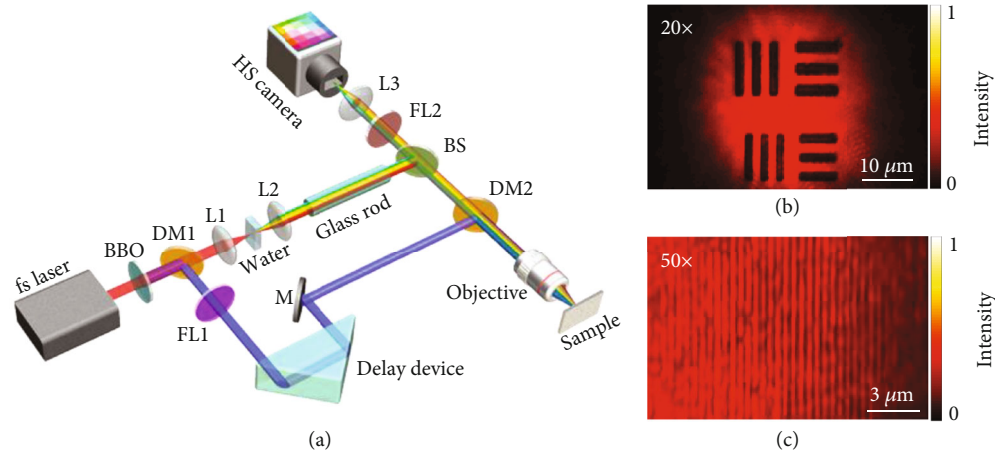
FIGURE 1: Configuration of CSMUP. (a) Experimental device of CSMUP. (b) Imaging a 1951 USAF resolution test target with a 20× objective. (c) Imaging a grating of 1200 lp/mm with a 50× objective.

characterized in detail in Ref. [38]. Then the broadband laser is collimated with the glass rods with the total length of 60 cm to produce a positively chirped probe laser. Finally, the pump and probe lasers are collinearly combined by a beam splitter (BS) and another 567 nm long-pass dichroic mirror (DM2), and an objective (20×, NA 0.45) is used to focus the pump laser onto the gold surface. The probe laser reflected from the gold surface is collected by a hyperspectral camera (Ximea, MQ022HG-IM-SM5×5-NIR), which can obtain 25 spectrally resolved images with the wavelength range from 659 to 949 nm. A 660 nm long-pass filter (FL2) is placed in front of the hyperspectral camera to narrow the spectral range of the probe laser and block the scattered light from the pump laser. A delay device is used to precisely control the time delay between the pump and probe lasers. To avoid the influence of rear side boundary of gold on the ablation process, a 2 mm thick bulky gold (purity 99.99%) is selected as the measured sample; such a thickness is much larger than the optical and thermal penetration depth.

The spatial and temporal resolutions are two key parameters of CSMUP. Firstly, a 1951 USAF resolution test target is imaged to characterize the spatial resolution of CSMUP with a 20× objective. One of the 25 spectral images is selected and shown in Figure 1(b); here, the groups 7-5 and 7-6 are given, in which 7-6 is corresponding to the spatial resolution of 228 lp/mm. Obviously, these horizontal or vertical stripes can be clearly observed. In addition, a gold grating of 1200 lp/mm is also imaged by a 50× objective (NA 0.8) with the same method, as shown in Figure 1(c). Similarly, these stripes are also clearly displayed, which shows high imaging quality with the spatial scale being up to 833 nm. Secondly, the temporal resolution of CSMUP is characterized by measuring the temporal-spectral distribution of the chirped probe pulse with a streak camera, which has been described in our previous work [37]. The probe laser pulse duration is about 100 ps; thus, the frame rate is about 250 billion frames per second; that is, the average frame interval is 4 ps.

In the theoretical simulation, a 3D TTM-MD model is used to simulate the FLA process of gold, which combines the continuum-level description of the laser excitation of conduction band electrons followed by electron-phonon equilibration with the MD simulation techniques (details in Supplementary Note 2). The simulations are performed using the large-scale atomic/molecular massively parallel simulator (LAMMPS) platform [39]. Meanwhile, the 3D TTM-MD simulations are based on the embedded-atom method (EAM) potential developed by Norman et al. [40]. This potential takes into account the change in the physical properties of ion subsystem caused by the heating of the electron subsystem, and therefore it can ensure an adequate description of forces acting upon gold ions in a two-temperature state of the system. The initial orientation for the gold crystal is [1 0 0], [0 1 0], and [0 0 1] in the x-, y-, and z-directions. To simulate a free gold target irradiated by the femtosecond laser in the experimental environment and control the system pressure, the periodic boundary conditions are applied along the x- and y-directions; a free boundary is used at the gold sample surface, and a Langevin nonreflecting boundary (LNRB) condition [41] is employed to absorb the laser-induced pressure wave and undermine its reflective propagation. The region beyond LNRB boundary is modeled by the original TTM formulation, mimicking the heat transfer into the deeper bulk part of the gold sample. The dimensions of the 3D simulation system are 73.4 nm × 73.4 nm × 118 nm. The crystalline gold sample has a thickness of 40.8 nm, containing 13,024,800 atoms, and the spatial range along the z-direction is from $z = -40.8$ nm to 0 nm. After the laser irradiation, the ablated clusters or atoms in vapor phase approaching the top region of the simulation cell (i.e., $z > 75$ nm) are manually deleted in order to avoid these clusters crossing the top boundary and causing unreasonable impacts on the bottom of the gold sample. The number of atoms in each coarse-grained electronic temperature grid is around 350. The diameter of the laser spot is $d = 40$ nm. A thickness of three monoatomic layers is used as the LNRB layer.

3. Results and Discussion

The pump laser fluence is a critical factor to affect the ablation process of gold, and therefore the ablation threshold of the gold is first determined as $\Phi_{th} = 0.13$ J/cm^2 using a D^2 method (details in Supplementary Note 3 and Figure S4). Two pump lasers with the high fluence of 2.80 J/cm^2 (21.5Φ_{th}) and low fluence of 0.45 J/cm^2 (3.5Φ_{th}) are used to irradiate the gold; both fluences are above the ablation threshold. The transient images at different delay times captured by CSMUP are shown in Figures 2(a) and 2(c), where only 12 representative images are selected to display for each laser fluence. Due to the nonlinear chirp of the probe laser pulse caused by the high order dispersion of the glass rod and the nonequidistant distribution of the response bands in the hyperspectral camera, the temporal frame intervals are not exactly the same. For the high fluence, as shown in Figure 2(a), low-reflectivity region (LRR) with a decrease in the reflectivity is first induced on the material surface at 5.3 ps. Then, a dark region with strongly decreased reflectivity appears in the center of the LRR at 15.8 ps. Subsequently, the dark region gradually enlarges and finally, almost covers the whole LRR at 94.3 ps. For the low fluence, as shown in Figure 2(c), the FLA process is similar to that in the high fluence. That is, an LRR is first created, and then, a dark region forms in the center of the LRR. However, the appearance of the dark region is obviously later at 29.1 ps. Moreover, the sizes of the two regions are much smaller, and their boundaries are blurry, which is due to the peripheral fluence of the laser spot falling below the ablation threshold.

To explain the morphological evolution of the gold during FLA processes observed in Figures 2(a) and 2(c), the 3D TTM-MD model is used to simulate the time-resolved atomic motions and matter removal process of the gold after the irradiation of a femtosecond laser pulse, and the simulated results in an aerial view are shown in Figures 2(b) and 2(d). Here, the laser pulse width is set to 100 fs, and the average absorbed fluences are set to 2.80 J/cm^2 and 0.45 J/cm^2, respectively; the parameters are the same as those in experiment. In our simulations, the temporal interval is set to 5 ps, and the atoms are labelled with different colors according to their positions along the z-direction. The gold surface is defined as the depth of 0 nm. To compare with the experimentally observed transient morphology more clearly, we remove the ejected clusters in Figures 2(b) and 2(d) that are completely detached from the gold due to the laser pulse irradiation (see Video 1 for the complete visual comparison). For the high fluence, as shown in Figure 2(b), the gold has been melted within the first 10 ps, and the average height of the atoms near the surface increases due to the thermal expansion. At 15 ps, an ablation crater at negative height can be faintly seen under the center of the expanding surface material, and the crater gradually becomes larger after 20 ps. For the low fluence, as shown in Figure 2(d), the appearance of the crater is postponed to 30 ps, which is later than 15 ps compared with that for the high fluence. In addition, the crater size is significantly reduced. By comparing the experimental

and simulation results, it can be found that the evolutions of the dark region in Figures 2(a) and 2(c) are very consistent with the evolutions of the ablation crater in Figures 2(b) and 2(d), respectively. The consistency is mainly reflected in the following three aspects: first, the occurrence time of the ablation crater predicted in simulation is consistent with that of the dark region observed in experiment. For the high fluence, the experimental result in Figure 2(a) shows that the dark region starts to appear on the gold surface obviously at 15.8 ps, and correspondingly, the simulation result in Figure 2(b) shows that the crater can be observed since 15 ps. Similarly, for the low fluence, the experimental result in Figure 2(c) shows that the dark region starts to appear on the gold surface obviously at 29.1 ps, and the simulation result in Figure 2(d) shows that the crater can be observed since 30 ps. Second, the size evolution of the ablation crater predicted by the simulation is consistent with that of the dark region observed experimentally. In experiments, the size of the dark region has gradually increased since its appearance, and the size of the dark region formed under high-fluence laser irradiation is larger than that under the low-fluence laser irradiation. Similarly, the evolutions of the ablation craters predicted from the simulations have the same characteristics. Third, the size ratio of the ablation crater at 95 ps predicted by the simulation is consistent with that of the dark region observed experimentally. Here, the diameter of the dark region in experiments (or simulations) is $d1 = 40.8$ μm (or $d2 = 27.5$ nm) for the high fluence and $d3 = 25.6$ μm (or $d4 = 17.0$ nm) for the low fluence. Obviously, the two size ratios of $d1/d3$ and $d2/d4$ show a close agreement. In general, the ultrafast morphological dynamics in the aerial view obtained through theoretical simulations are well consistent with the ultrafast reflectivity dynamics obtained through experimental measurements. It is worth noting that there exists a gap between the sizes of the laser spot in experiments and simulations. To verify the validity of our simulations, three pump lasers with different spot sizes are employed to irradiate the gold, and all the calculation results show a high consistency in the size ratio between the dark region and ablation carter (details in Supplementary Note 4 and Figure S5).

Next, we further explain the transient reflectivity evolution of the gold observed in experimental results of Figures 2(a) and 2(c) by side views of the simulated atomic configuration results, as shown in Figure 3. For the high fluence in Figure 3(a), the material close to the surface undergoes rapid thermal expansion along the laser incidence direction for the first 10 ps. The thermal expansion will cause a fast decrease in the material density below the surface, which leads to a decrease of free electron density. The decrease of free electron density will induce the reduction of the plasma frequency [42], and, finally, change the dielectric function of the material. It is just the change of the dielectric function that reduces the reflectivity of the material to the probe laser, which results in the emergence of the LRR within 9.0 ps in Figure 2(a) [43, 44]. Then, the surface layer in the center of the expanded material starts to eject at 15 ps, and the cluster ejection will lead to the gradual formation of the ablation crater. In addition, the ejected
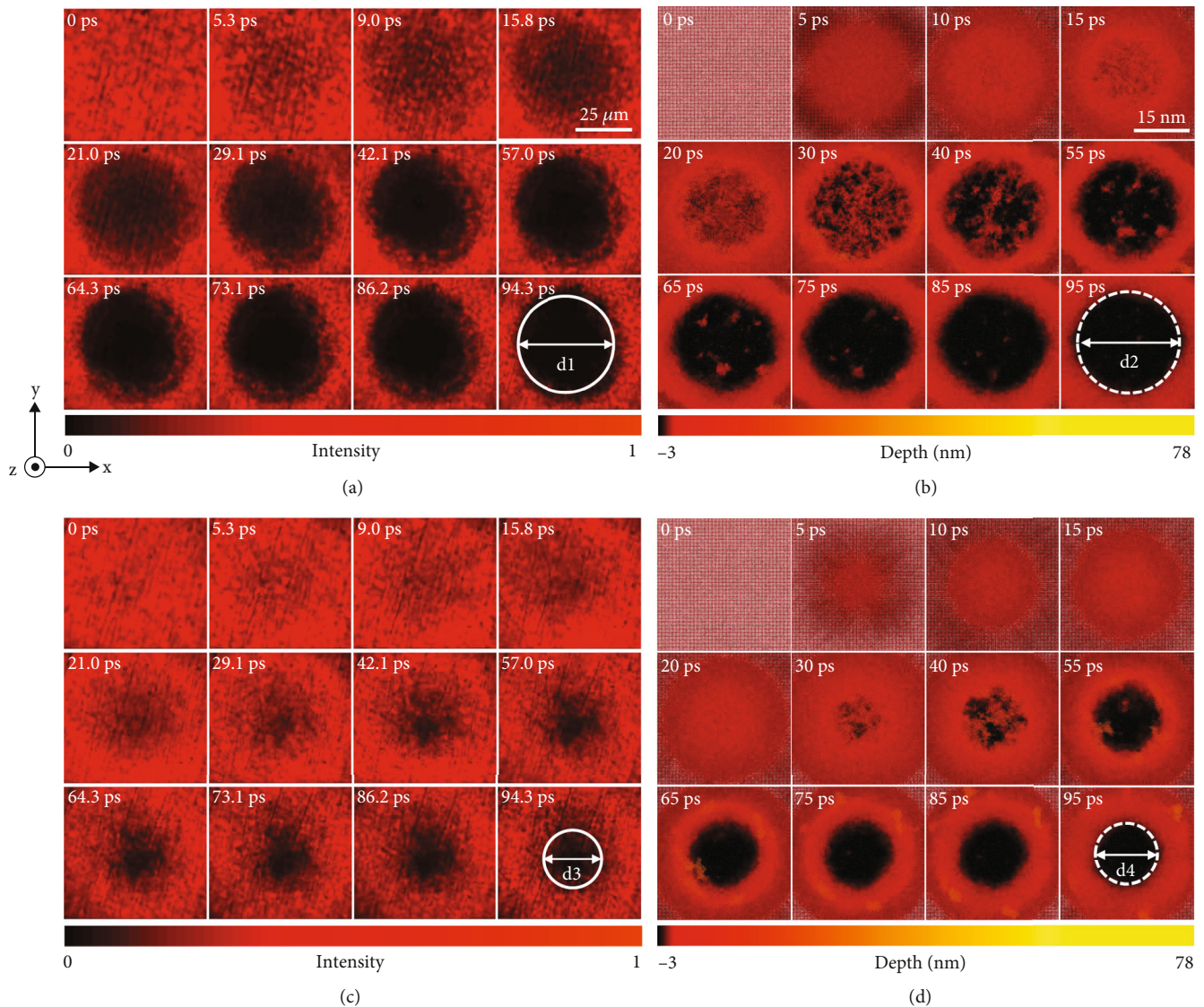
FIGURE 2: Experimental and theoretical simulation results. Representative recorded images of bulky gold target by CSMUP with the laser fluences of 2.80 (a) and 0.45 J/cm² (c), and simulated aerial-view snapshots of atomic configurations by 3D TTM-MD simulations with the absorbed fluences of 2.80 (b) and 0.45 J/cm² (d). Here, the solid and dashed circles denote the estimated boundaries for experiments and simulations.

clusters can absorb and scatter the probe photons, leading to a further decrease in reflectivity. Considering the limitations of the spatial resolution of the CSMUP system and the normal incidence of the probe laser, the clusters cannot be captured experimentally, only a strong decrease of the transient reflectivity caused by the cluster ejection and the ablation crater formation is observed at 15.8 ps from Figure 2(a), i.e., a dark region starts to appear in the center of the LRR. Subsequently, the increase in ejected material induces the expansion of the dark region, and the dense ejected clusters cannot be penetrated by most of the probe laser. Even if a small fraction of the probe photons can pass through the dense clusters, they are also scattered by the crater beneath the clusters. These effects lead to the pump laser irradiation region evolving into an almost black, nonreflective region in Figure 2(a). For the low fluence, as shown in Figure 3(b), the

expansion rate of material near the surface in the first 20 ps is significantly lower than that of the high fluence in Figure 3(a), so the decrease of transient reflectivity in the initial stage in Figure 2(c) is much smaller than that of the high fluence in Figure 2(a). Then, the cluster ejection begins at 30 ps, which is highly consistent with the earliest appearance of the dark region at 29.1 ps in Figure 2(c). After 30 ps, fewer clusters are ejected; the size of the dark region and the decrease in the reflectivity are smaller in experiment.

As a quantitative analysis, the temporal evolution of normalized reflectivity change, i.e., $\Delta R/R_0$ ($\Delta R = R - R_0$), is extracted from Figures 2(a) and 2(c), where R and R_0 represent the reflectivity with and without the pump laser irradiation, respectively. The extracted results in the high and low fluences are shown in Figure 4(a). It can be seen that, after the femtosecond laser irradiation, the reflectivity
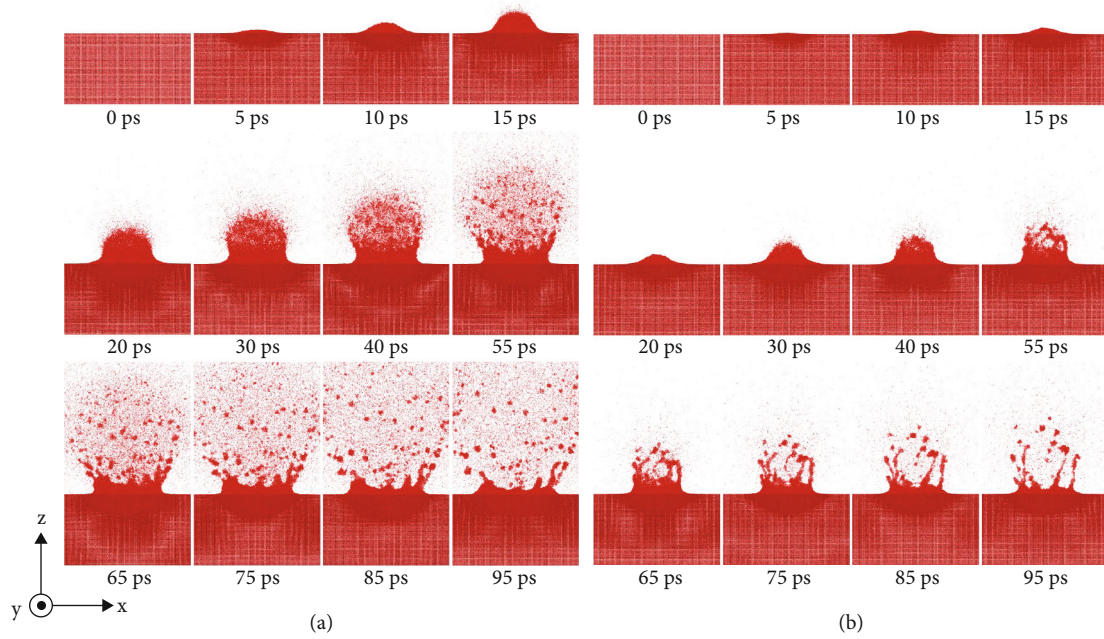
FIGURE 3: The side views of the simulated atomic configuration results. Representative simulated side views of atomic configurations by 3D TTM-MD simulations with the absorbed fluences of 2.80 (a) and 0.45 J/cm^2 (b).
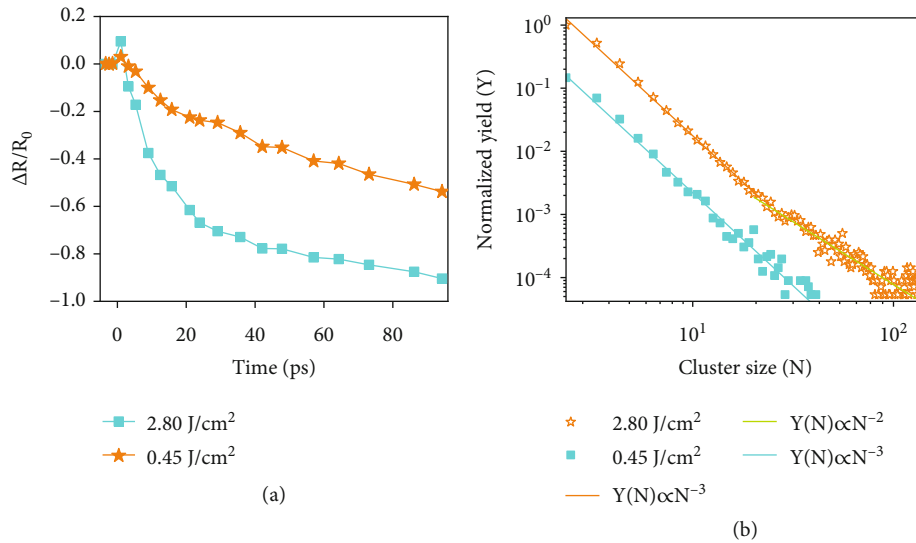

FIGURE 4: The temporal evolution of normalized reflectivity change and size distributions of the ejected clusters. (a) Temporal evolutions of normalized reflectivity changes $\Delta R/R_0$ extracted from the experimental results. (b) Cluster size distributions in the ablation plume extracted from the simulated results.

of the gold surface has a slight increase within a few picoseconds, which is due to the thermal excitation of the d-band electrons of gold induced by the 400 nm pump laser [45, 46]. Subsequently, $\Delta R/R_0$ shows an obvious decrease, but the evolution behavior is different for the high and low fluences. For the high fluence, $\Delta R/R_0$ first undergoes a rapid decrease to -0.71 within 21 ps. After 21 ps, the decrease of $\Delta R/R_0$ slows down, which reaches -0.91 at 94.3 ps. For the low fluence, $\Delta R/R_0$ maintains a monotonical decrease with a low slope throughout the evolution

process, and, finally, it only reaches -0.50. Therefore, it can be speculated that the FLA processes of gold in the high and low fluences should result from different physical mechanisms. In addition, the size distributions of the ejected clusters in the high and low fluences are also calculated from Figure 3. The cluster size distribution in the period of 65-95 ps after the laser irradiation is shown in Figure 4(b), where the horizontal axis is the cluster size, defined as the number of gold atoms contained in the cluster, and the vertical axis is the average ejection yield,
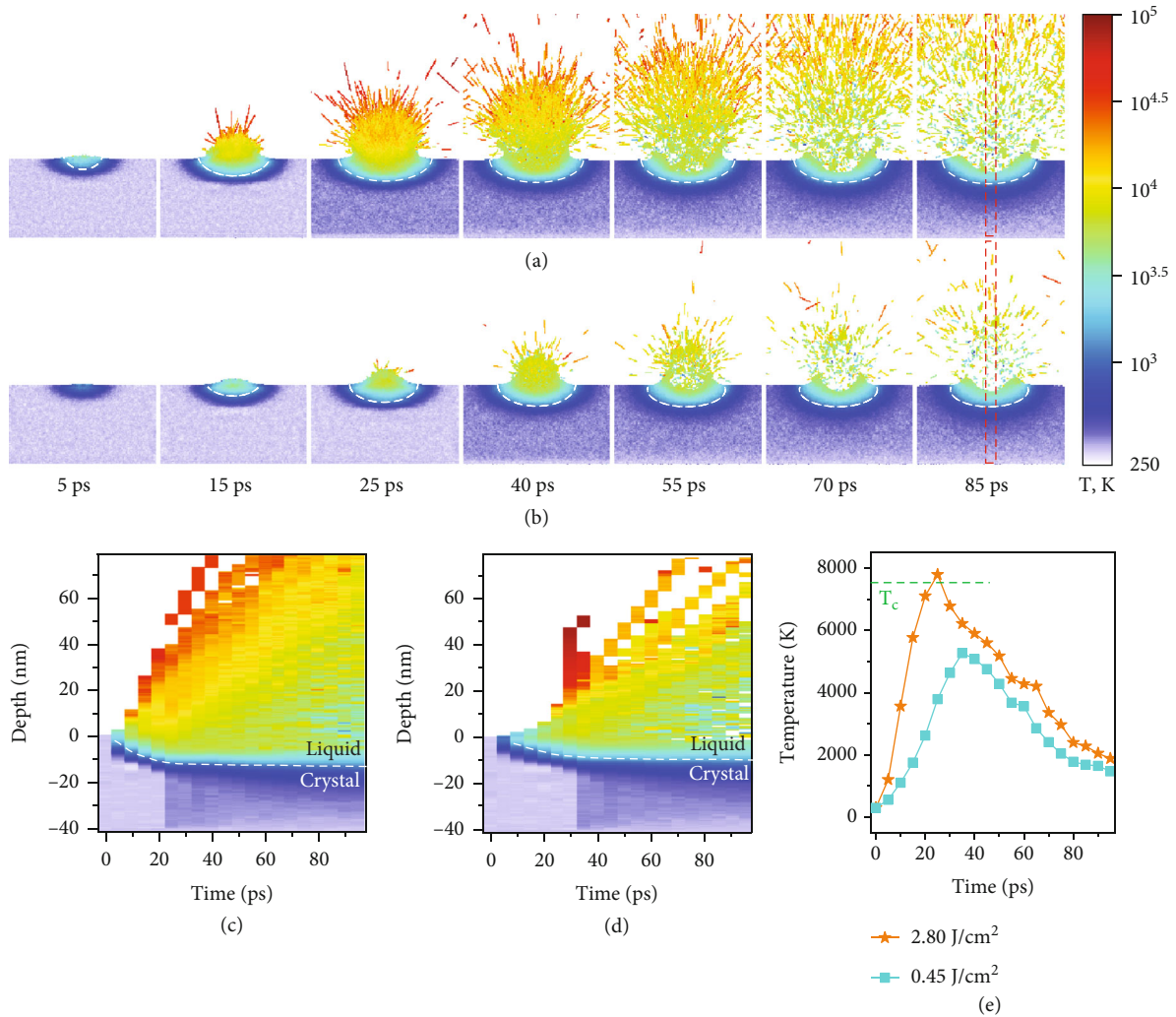
FIGURE 5: Spatiotemporal evolutions of lattice temperature. Representative simulated snapshots of lattice temperature by 3D TTM-MD simulations in the absorbed fluences of 2.80 (a) and 0.45 J/cm^2 (b). Contour plots of lattice temperature predicted in 3D TTM-MD simulations in the absorbed fluences of 2.80 (c) and 0.45 J/cm^2 (d). Temporal evolutions of average temperatures in the center of the molten pool (e). Here, the white and olive dashed lines denote the liquid-crystal interface and thermodynamical critical temperature T_c.

defined as the average number of clusters. Here, the yield is normalized to the number of minimum clusters. In double-logarithmic scale, the cluster size distribution can be better described by the power law $Y(N) \sim N^{-\tau}$. For the high fluence of 2.80 J/cm^2, the exponent of the low-mass cluster (atomic number < 20) $\tau = 3$ is larger than that of the high-mass cluster (atomic number > 20) $\tau = 2$, which means that the decay of the probability is much slower in the high-mass region of the distribution. In contrast, for the low fluence of 0.45 J/cm^2, the exponent τ for the region capable of producing a statistically significant number of clusters is kept at 2. Considering that there is a top absorption layer at the height of 78 nm, the atoms approaching this absorption layer are deleted in simulations. For the high fluence, a total of about 22,430 atoms are deleted. Compared to such a large base of approximate 10^6 atoms, it is believed that the atomic deletion does not affect the size distribution of the clusters. Referring to the detailed analysis in previous theoretical studies [47, 48],

here the FLA process in the high fluence probably contains a rather drastic ultrafast dynamics compared to that in the low fluence.

In order to verify above speculation for the FLA processes with different physical mechanisms in the high and low fluences, the spatiotemporal evolutions of lattice temperature, stress, and pressure are analyzed based on 3D TTM-MD simulations (see Video 2 for the complete temporal evolutions), where the 'lattice temperature' extends to the temperature of the out-of-equilibrium ionic subsystem. Besides, the details for calculating the 'stress' and 'pressure' can be found in Supplementary Note 5. Figures 5(a) and 5(b) show the representative snapshots of the lattice temperature and atomic motion trajectories for a sliced layer with a thickness of 2 nm along the y-direction in the high and low fluences, respectively. The excited atoms go through significant eruption that depends on the absorbed fluence, and the temperature of these atoms will rapidly rise to thousands of K and even higher. Moreover, the temperature distribution
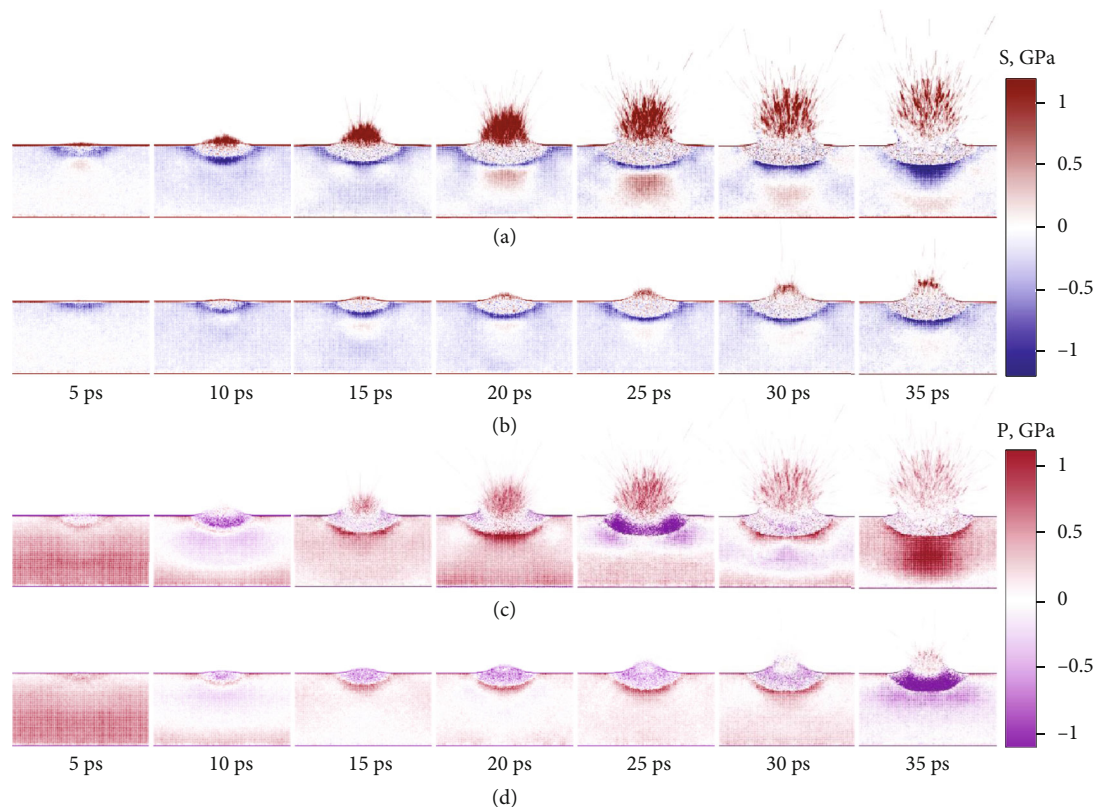
FIGURE 6: Spatiotemporal evolutions of stress and pressure. Simulated snapshots of stress (top row) and pressure (bottom row) in the early 35 ps by 3D TTM-MD simulations with the absorbed fluences of 2.80 (a, c), and 0.45 J/cm^2 (b, d) (Video 2, MP4, 2.4 MB).

shows an ascent gradient with the increase of the height above the surface of gold target throughout 100 ps, which indicates that the earlier erupted material obtains the higher kinetic energy. For the high fluence, as shown in Figure 5(a), lens-like-shaped molten pool in liquid phase has been established in the first 5 ps, where a white dotted curve indicates the liquid-crystal interface in each snapshot. Then, the molten pool expands due to the faster increase of the temperature within 25 ps. Meanwhile, a material eruption occurs, and the superficial atoms in the molten pool starts to separate from the gold target within 15 ps. Subsequently, the melt undergoes violent explosive decomposition with a large number of particles and clusters spewing out. For the low fluence, as shown in Figure 5(b), the size of the molten pool is significantly reduced due to the slower increase of the temperature, and the continuous unbroken liquid surface leads to the expansion of the molten pool in the form of a bubble (or a liquid film covering) with a time span of about 20 ps (from 5 to 25 ps). In addition, the subsequent melt decomposition and atomic eruption processes are milder, where fewer particles and clusters are ejected and a thinner plume is formed. Figures 5(c) and 5(d) present the contour plots of spatiotemporal evolution of lattice temperature in the high and low fluences, respectively. Here, a region with a width of 10 nm (red dotted box) in the center of the molten pool along the x-direction is selected and divided into 0.5 nm thick layers along the z-direction to calculate the average temperature for layers, as shown in Figures 5(a)

and 5(b). In both the high and low fluences, the gold target undergoes rapid melting within the first 30 ps, and the liquid-crystal interface (white dotted line) rapidly moves downward. After that, the melting and interface movement almost keep unchanged, which can be considered as the slower component. Compared with the low fluence, the melting front moves faster and the melting depth is deeper in the high fluence. Generally, the faster component of the melting results from the homogeneous nucleation and growth of multiple liquid regions inside the superheated crystal, while the slower component refers to the propagation of the liquid-crystal interface deeper into the gold target [49]. For further quantitative analysis, the temporal evolution of the average temperature within the height of -5 nm to 5 nm, corresponding to the core ablated region, is extracted from the contour plots in Figures 5(c) and 5(d), and the results are shown in Figure 5(e). In the high fluence, the temperature of this region rapidly rises within 30 ps and reaches a maximum of 7790 K, which exceeds the thermodynamic critical temperature of gold (i.e., $T_c = 7670$ K as indicated by the olive dotted line) [50]. In addition, the FLA process is accompanied by violent explosive eruption, and therefore we believe that the phase explosion is the most likely ablation mechanism. However, for the low fluence, the temperature in the center of the molten pool only reaches the peak value of 5268 K at 35 ps, which is far below the threshold temperature for phase explosion of 0.9 T_c [51]. Therefore, the time-resolved stress and pressure evolutions

are worth being studied to further explore the ablation mechanism.

The spatiotemporal evolutions of stress and pressure fields in the early 35 ps under the high and low fluences are shown in Figure 6, which are corresponding to the period of lattice temperature elevation. For the high fluence, as shown in Figures 6(a) and 6(c), the size of the lens-like-shaped molten pool increases in the initial 15 ps, accompanied by the melting and vaporization phase transitions, which have been demonstrated in the temperature evolution of Figure 5(a). Both of the phase transitions require a larger spatial volume to reduce the particle number densities. The liquid-crystal interface expands downward, while the vaporized clusters eject upward, which result in extreme variations in the local mechanical conditions. It is noticed that intense negative stress is built in the curved region beneath the molten ablation crater, suggesting that the liquid-crystal interface is in a state of lateral tension. Moreover, a dipole structure in the stress field is formed in the crystal region close to the liquid-crystal interface after 15 ps, which indicates that a positive stress or compressive state is built in this region. In contrast to the stress field, the evolution of the pressure field in the lens-like-shaped molten pool shows more complicated changes, where the pressure field experiences significant descent to negative value for twice at 10 and 25 ps, respectively. Owing to the rapid temperature elevation, the first significant pressure descent occurs at 10 ps before obvious eruption occurs, despite the negative pressure is maintained for a rather short time. Then, during the initial eruption in 15-20 ps, a slightly positive pressure appears in the center of the molten pool, which may be related to the intense liquid-gas phase transition near the critical temperature. Furthermore, when a large number of vaporized clusters (or atoms) are ejected from the molten pool, the traction effect due to the collective eruption should be responsible for the abrupt pressure descent in this region, as can be observed from the snapshot of 25 ps in Figure 6(c). For the low fluence, as shown in Figures 6(b) and 6(d), the evolution of the mechanical field is more moderate compared with that for the high fluence. The liquid-vapor surface layer of the molten pool holds its integrity up to 20-25 ps without breaking, and the atoms in the lens-like-shaped molten pool (or bubble) suffer from negative pressure during this period. At 30 ps, the surface liquid layer breaks under the negative pressure environment, which indicates that the eruption takes over the competition as the temperature continuously rises. Similarly, an abrupt pressure descent can also be observed at 35 ps, indicating that the traction effect still plays an important role in the low fluence. By combining the temperature evolution in Figure 5(b), we infer that the photomechanical spallation mechanism mainly dominates the FLA process in the low fluence.

4. Conclusions

In summary, we have conducted a CSMUP technique to measure the single-pulse FLA process on a bulky gold in experiment, which solved the problem of multiple measurements for the pump-probe technique. Meanwhile, we have developed a 3D TTM-MD method to jointly investigate the FLA process of gold in accordance with the experimental conditions in theory, which could observe the time-resolved atomic motions as well as the thermodynamical fields of gold from 3D view. Our experimental and simulated results showed a fairly high agreement in the time-resolved morphologic dynamics, which confirmed the reliability of our experimental and theoretical methods. In addition, the spatiotemporal evolution of thermodynamical fields predicted by 3D TTM-MD simulations showed that the FLA process is due to the phase explosion at the high laser fluence while the photomechanical spallation at the low laser fluence. This work not only provides a technical basis for monitoring the ultrafast laser fabrication in real time but also is helpful for fully understanding the physical mechanism of the interaction between intense ultrafast laser and materials.

Data Availability

The data that support the plots within this article and other findings of the study are available from the corresponding authors upon reasonable request.

Conflicts of Interest

The authors declare that they have no known competing financial interests or personal relationships that could have appeared to influence the work reported in this paper.

Authors' Contributions

Jiali Yao and Dalong Qi contributed equally to this work.

Acknowledgments

Supplementary Materials

Supplementary 1. Supplemented sections: Supplementary Note 1 describes the experimental details. Figure S1 shows the spectrum of the broadband laser produced by focusing an intense femtosecond laser pulse with a central wavelength of 800 nm in water. Figure S2 shows the physical view of the glass rods used in the CSMUP system and the spectral-temporal distribution of the chirped probe pulse. Figure S3 shows the response curves of 25 spectral bands in the hyperspectral camera. Supplementary Note 2 describes the calculation method of TTM-MD model. Table S1 lists the specific calculation parameters. Supplementary Note 3 describes a method for measuring ablation threshold fluence of the gold target. Figure S4 shows the ablation area versus the single pulse energy. Supplementary Note 4 describes the effect of spot size on the TTM-MD simulation results. Figure S5 visualizes the simulation results under different size spot irradiation. Supplementary Note 5 describes the

calculation method of pressure and stress in TTM-MD simulations. The supplementary materials contain the additional references [52–62]. Supplementary 2. Supplemented animation: the supplemented MP4-file shows a sequence of Figure 2. Supplementary 3. Supplemented animation: the supplemented MP4-file shows a sequence of Figures 5 and 6, respectively. *(Supplementary Materials)*

References

[1] D. Spence, P. Kean, and W. Sibbett, "60-fsec pulse generation from a self-mode-locked Ti: sapphire laser," *Optics Letters*, vol. 16, no. 1, pp. 42–44, 1991.

[2] D. Forster, B. Jaggi, A. Michalowski, and B. Neuenschwander, "Review on experimental and theoretical investigations of ultra-short pulsed laser ablation of metals with burst pulses," *Materials*, vol. 14, no. 12, p. 3331, 2021.

[3] J. Kruger and W. Kautek, "Ultrashort pulse laser interaction with dielectrics and polymers," *Advances in Polymer Science*, vol. 168, pp. 247–289, 2004.

[4] P. Balling and J. Schou, "Femtosecond-laser ablation dynamics of dielectrics: basics and applications for thin films," *Reports on Progress in Physics*, vol. 76, no. 3, article 036502, 2013.

[5] C. Momma, B. Chichkov, S. Nolte et al., "Short-pulse laser ablation of solid targets," *Optics Communications*, vol. 129, pp. 134–142, 1996.

[6] H. Wang, M. He, H. Liu, and Y. Guan, "One-step fabrication of robust superhydrophobic steel surfaces with mechanical durability, thermal stability, and anti-icing function," *ACS Applied Materials & Interfaces*, vol. 11, no. 28, pp. 25586–25594, 2019.

[7] J. Cheng, C. Liu, S. Shang et al., "A review of ultrafast laser materials micromachining," *Optics and Laser Technology*, vol. 46, pp. 88–102, 2013.

[8] Z. Lei, Z. Tian, and Y. Chen, "Laser cleaning technology in industrial fields," *Laser and Optoelectronics Progress*, vol. 55, no. 3, p. 030005, 2018.

[9] I. Miyamoto, A. Horn, J. Gottmann, D. Wortmann, and F. Yoshino, "Fusion welding of glass using femtosecond laser pulses with high-repetition rates," *Journal of Laser Micro/Nanoengineering*, vol. 2, no. 1, pp. 57–63, 2007.

[10] A. Ancona, F. Röser, K. Rademaker, J. Limpert, S. Nolte, and A. Tünnermann, "High speed laser drilling of metals using a high repetition rate, high average power ultrafast fiber CPA system," *Optics Express*, vol. 16, no. 12, pp. 8958–8968, 2008.

[11] C. Li, J. Hu, L. Jiang et al., "Shaped femtosecond laser induced photoreduction for highly controllable au nanoparticles based on localized field enhancement and their SERS applications," *Nano*, vol. 9, no. 3, pp. 691–702, 2020.

[12] S. B. Moram, C. Byram, and V. R. Soma, "Gold-nanoparticle- and nanostar-loaded paper-based SERS substrates for sensing nanogram-level picric acid with a portable Raman spectrometer," *Bulletin of Materials Science*, vol. 43, no. 1, p. 53, 2020.

[13] W. Qian, T. Curry, Y. Che, and R. Kopelman, "Targeted delivery of peptide-conjugated biocompatible gold nanoparticles into cancer cell nucleus," *Proceedings of SPIE*, vol. 8595, no. 3, pp. 767–769, 2013.

[14] A. Trouiller, S. Hebie, F. El Bahhaj, T. Napporn, and P. Bertrand, "Chemistry for oncotheranostic gold nanoparticles," *European Journal of Medicinal Chemistry*, vol. 99, pp. 92–112, 2015.

[15] B. Della Ventura, R. Funari, K. Anoop et al., "Nano-machining of biosensor electrodes through gold nanoparticles deposition produced by femtosecond laser ablation," *Applied Physics B*, vol. 119, no. 3, pp. 497–501, 2015.

[16] X. Wang, F. Chen, H. Liu et al., "Fabrication of micro-gratings on Au-Cr thin film by femtosecond laser interference with different pulse durations," *Applied Surface Science*, vol. 255, no. 20, pp. 8483–8487, 2009.

[17] Y. Nakata, T. Okada, and M. Maeda, "Fabrication of dot matrix, comb, and nanowire structures using laser ablation by interfered femtosecond laser beams," *Applied Physics Letters*, vol. 81, no. 22, pp. 4239–4241, 2002.

[18] D. Wortmann, J. Koch, M. Reininghaus et al., "Experimental and theoretical investigation on fs-laser-induced nanostructure formation on thin gold films," *Journal of Laser Applications*, vol. 24, no. 4, p. 042017, 2012.

[19] I. Carrasco-Garcia, J. Vadillo, and J. Laserna, "Monitoring the dynamics of the surface deformation prior to the onset of plasma emission during femtosecond laser ablation of noble metals by time- resolved reflectivity microscopy," *Spectrochimica Acta Part B*, vol. 131, pp. 1–7, 2017.

[20] T. Pflug, J. Wang, M. Olbrich, M. Frank, and A. Horn, "Case study on the dynamics of ultrafast laser heating and ablation of gold thin films by ultrafast pump-probe reflectometry and ellipsometry," *Applied Physics A*, vol. 124, no. 2, p. article 116, 2018.

[21] K. Cheng, J. Liu, K. Cao et al., "Ultrafast dynamics of single-pulse femtosecond laser-induced periodic ripples on the surface of a gold film," *Physical Review B*, vol. 98, no. 18, p. ???, 2018.

[22] X. Jia and X. Zhao, "Numerical study of material decomposition in ultrafast laser interaction with metals," *Applied Surface Science*, vol. 463, pp. 781–790, 2019.

[23] X. Zhao and Y. Shin, "Femtosecond laser ablation of aluminum in vacuum and air at high laser intensity," *Applied Surface Science*, vol. 283, pp. 94–99, 2013.

[24] P. Lorazo, L. Lewis, and M. Meunier, "Short-pulse laser ablation of solids: from phase explosion to fragmentation," *Physical Review Letters*, vol. 91, no. 22, p. 225502, 2003.

[25] C. Schafer, H. Urbassek, and L. Zhigilei, "Metal ablation by picosecond laser pulses: a hybrid simulation," *Physical Review B*, vol. 66, no. 11, p. article 115404, 2002.

[26] D. Duffy and A. Rutherford, "Including the effects of electronic stopping and electron-ion interactions in radiation damage simulations," *Journal of Physics. Condensed Matter*, vol. 19, no. 1, p. 016207, 2007.

[27] K. Nakagawa, A. Iwasaki, Y. Oishi et al., "Sequentially timed all-optical mapping photography (STAMP)," *Nature Photonics*, vol. 8, no. 9, pp. 695–700, 2014.

[28] T. Suzuki, F. Isa, L. Fujii et al., "Sequentially timed all-optical mapping photography (STAMP) utilizing spectral filtering," *Optics Express*, vol. 23, no. 23, pp. 30512–30522, 2015.

[29] X. Zeng, S. Zheng, Y. Cai et al., "High-spatial-resolution ultrafast framing imaging at 15 trillion frames per second by optical parametric amplification," *Advanced Photonics*, vol. 2, no. 5, p. article 056002, 2020.

[30] J. Liang, P. Wang, L. Zhu, and L. Wang, "Single-shot stereo-polarimetric compressed ultrafast photography for light-speed observation of high-dimensional optical transients with picosecond resolution," *Nature Communications*, vol. 11, no. 1, p. article 5252, 2020.

[31] T. Suzuki, R. Hida, Y. Yamaguchi, K. Nakagawa, T. Saiki, and F. Kannari, "Single-shot 25-frame burst imaging of ultrafast phase transition of Ge2Sb2Te5with a sub-picosecond resolution," *Applied Physics Express*, vol. 10, no. 9, p. 092502, 2017.

[32] T. Suzuki, H. Nemoto, K. Takasawa, and F. Kannari, "1000-fps consecutive ultrafast 2D-burst imaging with a sub-nanosecond temporal resolution by a frequency-time encoding of SF-STAMP," *Applied Physics A*, vol. 126, no. 2, p. article 135, 2020.

[33] J. Xie, J. Yan, and D. Zhu, "Atomic simulation of irradiation of cu film using femtosecond laser with different pulse durations," *Journal of Laser Applications*, vol. 32, no. 2, p. 022016, 2020.

[34] Z. Zhang, Z. Yang, C. Wang, Q. Zhang, S. Zheng, and W. Xu, "Mechanisms of femtosecond laser ablation of Ni3Al: molecular dynamics study," *Optics and Laser Technology*, vol. 133, p. 106505, 2021.

[35] X. Wang, "Large-scale molecular dynamics simulation of surface nanostructuring with a laser-assisted scanning tunnelling microscope," *Journal of Physics D*, vol. 38, no. 11, pp. 1805–1823, 2005.

[36] S. Ivanov, Z. Lin, B. Rethfeld, G. M. O'Connor, T. J. Glynn, and L. V. Zhigilei, "Nanocrystalline structure of nanobump generated by localized photoexcitation of metal film," *Journal of Applied Physics*, vol. 107, no. 1, p. 013519, 2010.

[37] Y. Yao, Y. He, D. Qi et al., "Single-shot real-time ultrafast imaging of femtosecond laser fabrication," *ACS Photonics*, vol. 8, no. 3, pp. 738–744, 2021.

[38] F. Cao, C. Yang, D. Qi et al., "Single-shot spatiotemporal intensity measurement of picosecond laser pulses with compressed ultrafast photography," *Optics and Lasers in Engineering*, vol. 116, pp. 89–93, 2019.

[39] S. Plimpton, "Fast parallel algorithms for short-range molecular dynamics," *Journal of Computational Physics*, vol. 117, no. 1, pp. 1–19, 1995.

[40] G. Norman, S. Starikov, and V. Stegailov, "Atomistic simulation of laser ablation of gold: effect of pressure relaxation," *Journal of Experimental and Theoretical Physics*, vol. 114, no. 5, pp. 792–800, 2012.

[41] I. Gnilitskyi, M. Shugaev, T. White, and L. Zhigilei, "Mechanism of single-pulse ablative generation of laser-induced periodic surface structures," *Physical Review B*, vol. 96, no. 20, p. 205429, 2017.

[42] M. Povarnitsyn, N. Andreev, E. Apfelbaum et al., "A wide-range model for simulation of pump-probe experiments with metals," *Applied Surface Science*, vol. 258, no. 23, pp. 9480–9483, 2012.

[43] M. Spellauge, J. Winter, S. Rapp et al., "Influence of stress confinement, particle shielding and re-deposition on the ultrashort pulse laser ablation of metals revealed by ultrafast time-resolved experiments," *Applied Surface Science*, vol. 545, p. 148930, 2021.

[44] J. Winter, S. Rapp, M. Schmidt, and H. P. Huber, *Ultrafast laser energy deposition in copper revealed by simulation and experimental determination of optical properties with pump-probe ellipsometry*, Laser Applications in Microelectronic and Optoelectronic Manufacturing (LAMOM), 2017.

[45] J. Winter, S. Rapp, M. Schmidt, and H. P. Huber, "Ultrafast laser processing of copper: a comparative study of experimental and simulated transient optical properties," *Applied Surface Science*, vol. 417, pp. 2–15, 2017.

[46] N. Inogamov, V. Zhakhovskii, S. Ashitkov et al., "Two-temperature relaxation and melting after absorption of femtosecond laser pulse," *Applied Surface Science*, vol. 255, no. 24, pp. 9712–9716, 2009.

[47] L. Zhigilei, Z. Lin, and D. Ivanov, "Atomistic modeling of short pulse laser ablation of metals: connections between melting, spallation, and phase explosion," *Journal of Physical Chemistry C*, vol. 113, no. 27, pp. 11892–11906, 2009.

[48] C. Wu and L. Zhigilei, "Microscopic mechanisms of laser spallation and ablation of metal targets from large-scale molecular dynamics simulations," *Applied Physics A: Materials Science & Processing*, vol. 114, no. 1, pp. 11–32, 2014.

[49] D. Ivanov and L. Zhigilei, "Effect of pressure relaxation on the mechanisms of short-pulse laser melting," *Physical Review Letters*, vol. 91, no. 10, p. article 105701, 2003.

[50] M. Martynyuk, "Critical constants of metals," *Russian Journal of Physical Chemistry*, vol. 57, pp. 494–501, 1983.

[51] A. Miotello and R. Kelly, "Laser-induced phase explosion: new physical problems when a condensed phase approaches the thermodynamic critical temperature," *Applied Physics A*, vol. 69, no. 7, pp. S67–S73, 1999.

[52] D. Ivanov and L. Zhigilei, "Combined atomistic-continuum modeling of short-pulse laser melting and disintegration of metal films," *Physical Review B*, vol. 68, no. 6, p. article 064114, 2003.

[53] J. Chen, D. Tzou, and J. Beraun, "A semiclassical two-temperature model for ultrafast laser heating," *International Journal of Heat and Mass Transfer*, vol. 49, no. 1-2, pp. 307–316, 2006.

[54] L. Falkovsky and E. Mishchenko, "Electron-lattice kinetics of metals heated by ultrashort laser pulses," *Journal of Experimental and Theoretical Physics*, vol. 88, no. 1, pp. 84–88, 1999.

[55] Z. Lin, L. Zhigilei, and V. Celli, "Electron-phonon coupling and electron heat capacity of metals under conditions of strong electron-phonon nonequilibrium," *Physical Review B*, vol. 77, no. 7, p. article 075133, 2008.

[56] G. Norman, S. Starikov, V. Stegailov, I. Saitov, and P. Zhilyaev, "Atomistic modeling of warm dense matter in the two-temperature state," *Contributions to Plasma Physics*, vol. 53, no. 2, pp. 129–139, 2013.

[57] A. Rutherford and D. Duffy, "The effect of electron-ion interactions on radiation damage simulations," *Journal of Physics. Condensed Matter*, vol. 19, no. 49, p. 496201, 2007.

[58] R. Stoller, M. Toloczko, G. Was, A. G. Certain, S. Dwaraknath, and F. A. Garner, "On the use of SRIM for computing radiation damage exposure," *Nuclear Instruments and Methods in Physics Research Section B*, vol. 310, pp. 75–80, 2013.

[59] J. Ziegler, M. Ziegler, and J. Biersack, "SRIM - the stopping and range of ions in matter (2010)," *Nuclear Instruments and Methods in Physics Research Section B*, vol. 268, no. 11-12, pp. 1818–1823, 2010.

[60] G. Fuentes, E. Elizalde, F. Yubero, and J. Sanz, "Electron inelastic mean free path for Ti, TiC, TiN and TiO2 as determined by quantitative reflection electron energy-loss spectroscopy," *Surface and Interface Analysis*, vol. 33, no. 3, pp. 230–237, 2002.

[61] D. Gall, "Electron mean free path in elemental metals," *Journal of Applied Physics*, vol. 119, no. 8, p. 085101, 2016.

[62] J. Natoli, L. Gallais, H. Akhouayri, and C. Amra, "Laser-induced damage of materials in bulk, thin-film, and liquid forms," *Applied Optics*, vol. 41, no. 16, pp. 3156–3166, 2002.